Helicities of Electron Magnetohydrodynamic Currents and Fields in Plasmas

R. L. Stenzel, J. M. Urrutia, and C. L. Rousculp
Department of Physics, University of California, Los Angeles, California 90024-1547
(Received 16 March 1994; revised manuscript received 14 September 1994)

Transient plasma currents are excited with pulsed electrodes in a large laboratory plasma in a parameter regime characterized by electron magnetohydrodynamics ($\omega_{ce}^{-1} \ll t_{\text{pulse}}/2\pi \ll \omega_{ci}^{-1}$). The combination of Hall currents and field-aligned currents gives rise to three-dimensional vortices whose helicity is manifested by linked and knotted current and field lines. The relation between magnetic helicity, $\int \mathbf{A} \cdot \mathbf{B}\, dV$, current helicity, $\int \mathbf{J} \cdot \mathbf{B}\, dV$, and their transport properties are investigated.

PACS numbers: 52.35.Hr, 52.30.Bt, 52.40.Db, 52.70.Ds

The topology of magnetic fields in plasmas is a topic of fundamental importance in fusion and space plasmas. While the attention is commonly focused on magnetohydrodynamic (MHD) plasmas [1], more recently the regime of electron MHD (EMHD, i.e., magnetized electrons, unmagnetized ions) has become of interest with its many applications such as plasma opening switches, electrodynamic tethers, and plasma releases in space [2–5]. In EMHD, Ohm's law is dominated by electron Hall currents. Under such conditions, the fields frequently have a three-dimensional (3D) topology, which rarely have been measured and compared to theory. One method to quantitatively describe the field topology of a 3D vector field, $\nabla \times \mathbf{X}$, is through its helicity, $H = \int \mathbf{X} \cdot (\nabla \times \mathbf{X})\, dV$ [6]. It is a measure for linkage and knotting of field lines, as well as for internal twisting and kinking of flux tubes. Magnetic helicity, $\int \mathbf{A} \cdot \mathbf{B}\, dV$, is conserved for frozen-in $\mathbf{B}$ fields in ideal plasmas, as is the fluid helicity, $\int \mathbf{v} \cdot (\nabla \times \mathbf{v})\, dV$, in ideal hydrodynamics [1]. In certain nonideal plasmas, Taylor [7] conjectured that magnetic helicity remains constant while the magnetic energy decays. In this Letter, we measure the helicities of the vector fields $\nabla \times \mathbf{A} = \mathbf{B}$ and $\nabla \times \mathbf{B} = \mu_0 \mathbf{J} \approx -n_e e \mathbf{v}_e$, and explain their transport properties via Maxwell's equations and Ohm's law appropriate to EMHD. The vector potential $\mathbf{A}$ and current density $\mathbf{J}$ are derived from direct probe measurements of $\mathbf{B}(\mathbf{r}, t)$ at more than 10 000 positions in a simple basic physics experiment: A pulsed current is drawn to a positively biased disk electrode inserted axially into a large, uniform, quiescent magnetoplasma. In the present parameter regime ($\omega_{pe} \gg \omega_{ce} \gg \omega \approx 2\pi/t_{\text{pulse}} \gg \omega_{ci}$), the current pulses are transported by low frequency whistler wave packets [8], as demonstrated by Fourier transforming $\mathbf{B}(\mathbf{r}, t)$ to $\mathbf{B}(\mathbf{k}, \omega)$, and observing the spectral distribution to lie on the refractive index surface of oblique whistlers [9]. Both $\mathbf{B}$ and $\mathbf{J}$ exhibit positive helicity due to right-handed linkage of azimuthal Hall currents and field-aligned currents. The latter close like the fields of a short solenoid, such that the resultant topology is that of a 3D vortex (Hill's vortex, spheromak [10]). Trefoil knots are observed in lines of $\mathbf{A}$, $\mathbf{B}$, and $\mathbf{J}$. During the pulse propagation, both energy and helicity decay at the *same* rate, but the normalized helicity (e.g., $\mathbf{J} \cdot \mathbf{B}/JB = \cos\varphi$) remains constant. Hence, the topology does not change. Helicity transport studies show that magnetic helicity is volume generated, while current helicity is injected by the electrode. Dissipation is by collisions rather than Landau damping as in helicons [11]. On time scales short compared to diffusion times, the magnetic field is shown to be frozen to the electron fluid ($\mathbf{B} \propto \mathbf{J} \propto \mathbf{v}_e$). The electromagnetic fields exert essentially no force on the electron fluid, $\mathbf{f} = n_e e \mathbf{E} + \mathbf{J} \times (\mathbf{B} + \mathbf{B}_0) \approx 0$ [12].

The experimental setup sketched in Fig. 1 consists of a large (1 m diam × 2.5 m length) afterglow plasma column ($n_e = 9 \times 10^{10}$ cm^{-3}, $kT_e = 0.8$ eV, $B_0 = 10$ G, Ar, $p_n = 3 \times 10^{-4}$ Torr) into which a disk electrode (4 cm diam) with an insulated shaft is axially inserted. A positive current pulse ($t_{\text{pulse}} = 150$ ns, $I_{\max} = 50$ mA) is applied using the chamber wall as the ion collecting return electrode. With a triple magnetic probe (1 cm diam) movable in three dimensions, the time-dependent magnetic field $(B_x, B_y, B_z)(x, y, z, t)$ is recorded from repeated experiments in the central plasma volume (26 cm $\perp \mathbf{B}_0$, 55 cm $\parallel \mathbf{B}_0$) with $\Delta t = 10$ ns time resolution and digitally stored. The current density is calculated from Ampère's law, $\mathbf{J}(\mathbf{r}, t) = \nabla \times \mathbf{B}(\mathbf{r}, t)/\mu_0$, where $\mathbf{J}$ includes the negligible vacuum displacement current ($\epsilon_0 |\partial \mathbf{E}/\partial t| / |\mathbf{J}| \approx \epsilon_0 \omega E/\sigma_H E = \omega \omega_{ce}/\omega_{pe}^2 \approx 10^{-5}$, when Hall currents dominate as shown below). The current penetrates from the electrode into the plasma along $\mathbf{B}_0$ at a charac-

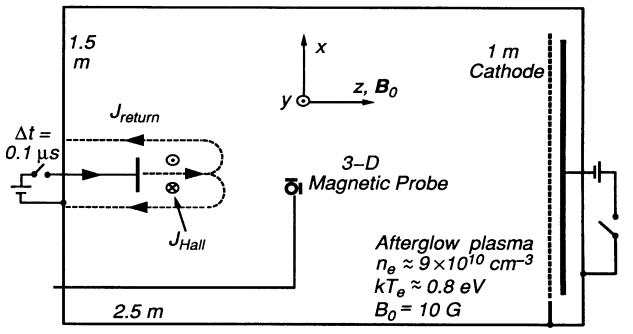

FIG. 1. Experimental setup, parameters, and pulsed currents in a magnetoplasma.

 0031-9007/95/74(5)/702(4)$06.00

teristic wave speed ($v_\parallel = v_{\text{whistler}} \approx 1.4 \times 10^8$ cm/s) and closes via induced return currents to the chamber wall. The collection of electrons from the flux tube of the electrode leads to a radial space charge electric field, which gives rise to azimuthal Hall currents because ion $\mathbf{E} \times \mathbf{B}_0$ drifts are negligible in EMHD. When the applied current pulse has ended, the plasma current lines detach from the electrodes, close within the plasma volume, and propagate along $\mathbf{B}_0$ with little spread across $\mathbf{B}_0$.

Figure 2 presents a snapshot of typical field topologies at a time after the end of the applied current pulse. At this time, the perturbation has propagated to the middle of the measurement volume. The vector potential $\mathbf{A}$ obtained by solving $\nabla \times \mathbf{A} = \mathbf{B}$ in 3D $\mathbf{k}$ space ($\nabla \cdot \mathbf{A} = 0$, Coulomb gauge) is displayed in Fig. 2(a) as unit-vector fields in two orthogonal planes. An axial, solenoidal field is visible in the central y-z plane (x indicated by adjacent diamond), which is linked by an azimuthal (toroidal) field in the x-y plane (z shown by diamond). A typical "field line" of $\mathbf{A}$ of the combined 3D vortexlike field is shown in Fig. 2(b). It is knotted and twisted. Trefoil knots [1] are also observed in magnetic flux tubes and current density tubes because the field topologies of $\mathbf{A}(\mathbf{r})$, $\mathbf{B}(\mathbf{r})$, and $\mathbf{J}(\mathbf{r})$ are observed to be similar. This can be shown to be true to first order. Defining $\omega_{ce} = e\mathbf{B}_0/m_e$, Ohm's law can be written as

$$\mathbf{E} = \frac{m_e}{n_e e^2}\left(\mathbf{J} \times \boldsymbol{\omega}_{ce} + \frac{\partial \mathbf{J}}{\partial t} + \nu \mathbf{J}\right). \tag{1}$$

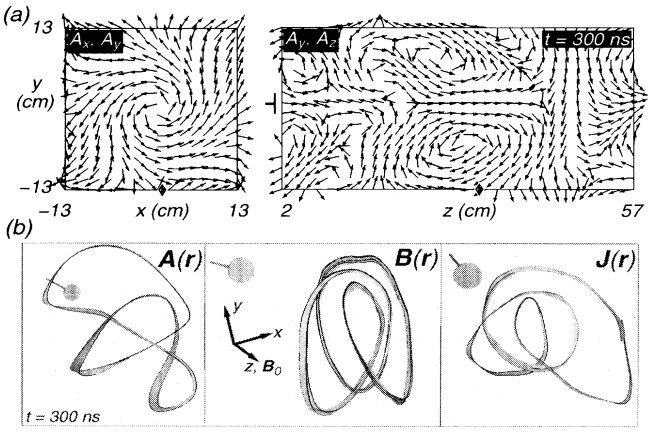

FIG. 2. Field topology of EMHD current pulses. (a) Snapshot of the vector potential field, $\mathbf{A}(\mathbf{r}, t = 0.3\ \mu\text{s})$, displayed as unit vectors in two orthogonal planes (third coordinate indicated by adjacent diamonds). The toroidal field in the transverse x-y plane is due to Hall currents. The solenoidal field in the center of the y-z plane is due to field-aligned currents excited earlier by the electrode. Both fields are linked to form a 3D vortex. A similar topology exists for $\mathbf{B} = \nabla \times \mathbf{A}$ and $\mathbf{J} = \nabla \times \mathbf{B}/\mu_0$. (b) Typical field lines of $\mathbf{A}$, $\mathbf{B}$, and $\mathbf{J}$ in the main vortex ($z \approx 30$ cm) displayed as "sheets" (two adjacent lines connected by a surface) or "tubes" (four lines started on the corners of a square, connected by sheets). The fields are internally twisted, knotted, writhed, and linked with other lines (not shown for clarity), i.e., they exhibit helicity.

For the EMHD regime, the Hall term is dominant, followed by the inertial and resistive terms ($\omega_{ce} = eB_0/m_e \gg \partial/\partial t \gg \nu$). Neglecting collisions, Faraday's law yields

$$\frac{\partial \mathbf{B}}{\partial t} = -\nabla \times \mathbf{E} \approx -\frac{m_e}{n_e e^2}\left(\boldsymbol{\omega}_{ce} \cdot \nabla \mathbf{J} + \nabla \times \frac{\partial \mathbf{J}}{\partial t}\right), \tag{2}$$

which, for $\omega_{ce} \cdot \nabla = \omega_{ce}\partial/\partial z \approx -(\omega_{ce}/v_\parallel)\partial/\partial t$, can be integrated to obtain

$$\mathbf{B} \approx \mathbf{J}/\sigma_H v_\parallel - \nabla \times \mathbf{J}/\sigma_H \omega_{ce}\,. \tag{3}$$

Since $\nabla \cdot \mathbf{A} = \nabla \cdot \mathbf{B} = 0$, inspection of Eq. (3) yields

$$\mathbf{A} \approx \mathbf{B}/\mu_0 \sigma_H v_\parallel - \mathbf{J}/\sigma_H \omega_{ce}\,, \tag{4}$$

where $\sigma_H = n_e e/B_0$ is the Hall conductivity. Hence, to first order $\mathbf{A}(\mathbf{r}) \propto \mathbf{B}(\mathbf{r}) \propto \mathbf{J}(\mathbf{r})$.

The helicity density of the $\mathbf{J}$ field, $h = \mathbf{J} \cdot \mathbf{B}(x = 0, y, z; t = 0.3\ \mu\text{s})$, shown in Fig. 3(a), exhibits a large positive pulse in the center, followed by smaller secondary pulses, which are induced by the primary vortex [also visible in Fig. 2(a)]. The magnetic helicity density, $\mathbf{A} \cdot \mathbf{B}$, has a similar distribution. When integrated over the transverse cross section, $\iint \mathbf{J} \cdot \mathbf{B}\, dx\, dy$, axial propagation and decay of helicity can be observed for the different pulses in a z-t diagram [Fig. 3(b)]. The first pulse carries most of the helicity, propagates at $v_\parallel \approx 1.4 \times 10^8$ cm/s, and decays within the volume. The typical amplitude decays along the propagation characteristics (line between diamonds, $z = v_\parallel t'$) is shown in Fig. 3(c). Magnetic energy (dashed line), current helicity (solid line), and magnetic helicity (not shown for clarity) decay at the same rate, since $\mathbf{A}(\mathbf{r}) \propto \mathbf{B}(\mathbf{r}) \propto \mathbf{J}(\mathbf{r})$, as shown above. However, the suitably normalized helicity, $\iint \mathbf{J} \cdot \mathbf{B}\, dx\, dy / \iint JB\, dx\, dy$, is constant and close to unity, indicating that the average angle between the vectors does not change. Thus, the topology does not change as the helicity decays.

Finally, integration along z of the data presented in Fig. 3(b) yields the total helicity in the measurement volume, $H = \int h\, dV$. This is shown in Fig. 4(a) for the magnetic field helicity and in Fig. 4(b) for the current density helicity (or electron fluid velocity). The temporal growth and decay of helicity during the passage of pulses through the volume can be analyzed for the helicities analogous to that of the energy, i.e., through Poynting's theorem ($\partial U_{em}/\partial t = -\int_S \mathbf{S} \cdot d\mathbf{a} - P_{\text{dissip}}$, where $\mathbf{S} = \mathbf{E} \times \mathbf{B}/\mu_0$). The time rate of change of the magnetic helicity can be expressed as

$$\dot{H}_B = -\int_S (\mathbf{E}_{\text{ind}} \times \mathbf{A} + 2\phi \mathbf{B}) \cdot d\mathbf{a} - 2\int \mathbf{E} \cdot \mathbf{B}\, dV\,, \tag{5}$$

where ϕ is the scalar potential [1,6]. The first integral describes the flux of magnetic helicity across closed surfaces, which consists of "ac" helicity injection [$\int_S (\partial \mathbf{A}/\partial t \times \mathbf{A}) \cdot d\mathbf{a}$] and "dc" helicity injection

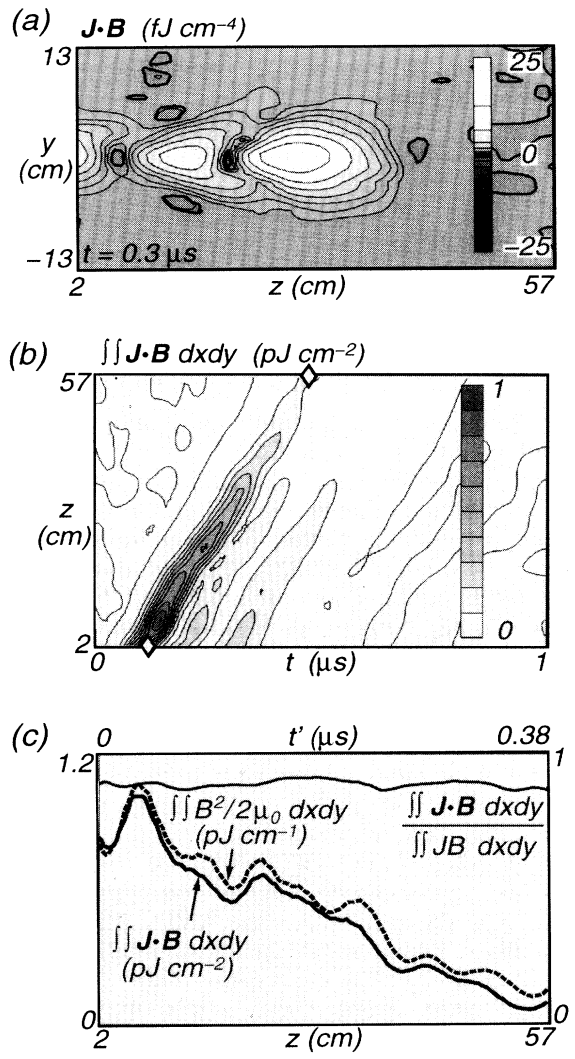

FIG. 3. Helicity density of the vector field $\mathbf{J} = -n_e e \mathbf{v}_e$, showing positive helicity for all current pulses: the primary in the center and induced, secondary ones on the left. The pulses propagate at $v_{\text{whistler}} \approx 1.4 \times 10^8$ cm/s along z ($\| \mathbf{B}_0$) (3 dB = factor of 2 per contour; ±8 contours; zero contour has double width). (b) Helicity density integrated over transverse cross section showing propagation, damping, and relative helicities of the three pulses. Variation of integration limits (not shown) indicate that damping is *not* due to transverse outflow. (c) Helicity amplitude of the first major pulse along its propagation characteristics, $z = v_{\|} t'$ [straight line between diamonds in (b)]. For comparison, the magnetic energy (dashed line) along the same characteristic is shown and found to exhibit a similar decay. However, the normalized helicity remains constant and close to unity, implying that $\mathbf{J}$ and $\mathbf{B}$ are, on the average, well aligned and their topologies do not change due to dissipation.

($-2 \int_S \phi \mathbf{B} \cdot d\mathbf{a}$). The second integral describes helicity generation and losses within the volume. These rates have been time integrated and displayed in Fig. 4(a). The ac-injected helicity is found to be negligible. The dc flux,

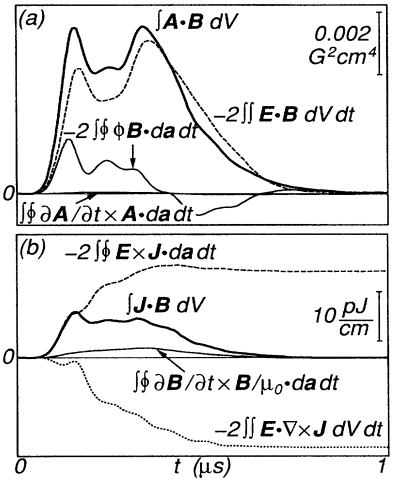

FIG. 4. Time dependence of the volume-integrated ($-13 < x, y < 13$ cm, $2 < z < 57$ cm) helicities and transport equation terms vs time. (a) Magnetic helicity, $\int\int \mathbf{A} \cdot \mathbf{B}\, dV$, mainly generated by volume sources, $-2 \int\int \mathbf{E} \cdot \mathbf{B}\, dV\, dt$, partly by dc injection, $-2 \int\int_S \phi \mathbf{B} \cdot d\mathbf{a}\, dt$, but insignificantly by ac injection, $\int\int_S (\partial \mathbf{A}/\partial t \times \mathbf{A}) \cdot d\mathbf{a}\, dt \approx 0$. Variation of the volume along z shows that there is no injection; by the electrode ($z = 0$), but only volume production near the source ($0 \le z \le 10$ cm). For $z \ge 10$ cm, volume dissipation occurs, and injection at $z_0 > 0$ is due to flow of helicity produced at $0 < z < z_0$. (b) Helicity of current density or electron fluid velocity, $\int \mathbf{J} \cdot \mathbf{B}\, dV$. This helicity is entirely injected from the electrode, mainly by the dc term, $-2 \int\int_S (\mathbf{E} \times \mathbf{J}) \cdot d\mathbf{a}\, dt \gg \int\int_S (\partial \mathbf{B}/\partial t \times \mathbf{B}) \cdot d\mathbf{a}\, dt$, and lost by volume dissipation, $-2 \int\int \mathbf{E} \cdot (\nabla \times \mathbf{J})\, dV\, dt < 0$. The transport resembles that of the energy since $\mathbf{E} \times \mathbf{J} \propto \mathbf{E} \times \mathbf{H} = \mathbf{S}$ (Poynting's vector) and $\mathbf{E} \cdot (\nabla \times \mathbf{J}) \propto \mathbf{E} \cdot \mathbf{J}$.

$-2 \int (\int_S \phi \mathbf{B} \cdot d\mathbf{a})\, dt$, exhibits both injection and outflow when the pulses enter and leave the volume. Most of the helicity is accounted for by volume production and losses which balance in time [$-2 \int (\int \mathbf{E} \cdot \mathbf{B}\, dV)\, dt \approx 0$ at $t \approx 1$ μs]. Further insight into the helicity transport is obtained by varying the axial starting position z for the volume/surface integration (not shown). As z is increased from its smallest value ($z = 2$ cm, Fig. 4, electrode at $z = 0$), the helicity injection rapidly increases, the volume production vanishes, and volume losses balance injection. Vice versa, extrapolation of this trend to $z = 0$ shows a negligible flux term, which is understandable since $\mathbf{B} \cdot d\mathbf{a} \to 0$ at the surface of the electrode. One must conclude that the magnetic helicity is created in the volume near the electrode ($0 < z < 10$ cm), transported, and gradually dissipated. The production of helicity near the electrode is evidence that Eq. (3) breaks down in the vicinity of the electrode. First order theory predicts that

$$-2 \iint \mathbf{E} \cdot \mathbf{B}\, dV dt \propto - \iint \frac{\partial \mathbf{J}}{\partial t} \cdot \mathbf{B}\, dV dt \propto -U_m < 0, \tag{6}$$

but the experimental observation is >0. The breakdown of Eq. (3) is due to the boundary conditions of $\mathbf{B}$ and $\mathbf{J}$ at the electrode ($\mathbf{B} \perp \mathbf{J}$).

The transport equation for H_J is given by

$$\dot{H}_J = \int \left[\mathbf{B} \cdot \left(\nabla \times \frac{\partial \mathbf{B}}{\partial t} \right) \Big/ \mu_0 - (\nabla \times \mathbf{E}) \cdot \mathbf{J} \right] dV$$

$$= \int_S \left(\frac{\partial \mathbf{B}}{\partial t} \times \mathbf{B}/\mu_0 - 2\mathbf{E} \times \mathbf{J} \right) \cdot d\mathbf{a} - 2 \times \int \mathbf{E} \cdot (\nabla \times \mathbf{J})\, dV , \quad (7)$$

where the helicity "Poynting's" vector has again an ac injection term, $\int_S (\partial \mathbf{B}/\partial t \times \mathbf{B}/\mu_0) \cdot d\mathbf{a}$, and a dc term, $-2 \int_S (\mathbf{E} \times \mathbf{J}) \cdot d\mathbf{a}$. Figure 4(b) shows the helicity contributions produced by each term. In contrast to the magnetic helicity, there is no volume generation but only volume dissipation. All the current helicity is injected, $-2 \int_S (\mathbf{E} \times \mathbf{J}) \cdot d\mathbf{a} \approx 2 \iint E_r J_\theta \, dx \, dy \approx 2\sigma_H \iint E_r^2 \, dx \, dy > 0$, where J_θ is derived from Eq. (1) by neglecting the inertial and resistive terms. This expression holds in the plasma but not at the surface of the electrode ($\mathbf{E} \parallel d\mathbf{a}$). Thus, the helicity flows around the electrode similar to Poynting's vector, $\mathbf{S}$.

Thus, in a Hall current-dominated regime ($|\mathbf{J}| / |\nabla \times \mathbf{J}| \gg v_\parallel/\omega_{ce}$), one has (i) $\mathbf{A} \propto \mathbf{B} \propto \mathbf{J}$ [Fig. 2(b)], hence $\mathbf{A} \cdot \mathbf{B} > 0$, $\mathbf{J} \cdot \mathbf{B} > 0$ [Fig. 3(a)]; (ii) normalized helicities constant and near unity [Fig. 3(c)]; (iii) constant helicity ratio, $\mathbf{J} \cdot \mathbf{B}/\mathbf{A} \cdot \mathbf{B} \approx \mu_0 (\sigma_H v_\parallel)^2$; (iv) helicity proportional to magnetic energy, $\mathbf{J} \cdot \mathbf{B} \approx 2L^{-1}(B^2/2\mu_0)$, where $L = (\mu_0 \sigma_H v_\parallel)^{-1}$; (v) ac helicity injection of $\mathbf{J} \cdot \mathbf{B}$ proportional to the Poynting's flux based on the small inductive electric field, $\int_S (\partial \mathbf{B}/\partial t \times \mathbf{B}/\mu_0) \cdot d\mathbf{a} \approx L^{-1} \int_S (\mathbf{E}_{\text{ind}} \times \mathbf{H}) \cdot d\mathbf{a}$; (vi) dc helicity injection of $\mathbf{J} \cdot \mathbf{B}$ proportional to the Poynting's flux,. $2 \int_S (\mathbf{E} \times \mathbf{J}) \cdot d\mathbf{a} \approx L^{-1} \int_S (\mathbf{E} \times \mathbf{H}) \cdot d\mathbf{a}$; and (vii) the volume term, $\int \mathbf{E} \cdot (\nabla \times \mathbf{J})\, dV \approx L^{-1} \int (\mathbf{E} \cdot \mathbf{J})\, dV$, whose time-integrated asymptotic value ($t \rightarrow 1$ μs) describes the total current helicity/energy dissipated. These simplified relations explain the observations qualitatively, but corrections for inertial and Ohmic terms improve quantitative comparisons.

In conclusion, first direct measurements of the helicity properties of a three-dimensional EMHD current system produced by a simple geometry have been presented. Helicity arises self-consistently from the linkage of Hall currents with field-aligned currents. The former are always produced by the latter since the immobile ions cannot neutralize the electron charge imbalances. The relation between helicities and their transport have been analyzed and explained by basic equations. These results are of intrinsic interest and of possible relevance to various EMHD applications, theories, and simulations.

The authors gratefully acknowledge support from Grants No. NSF PHY93-03821 and No. NASA NAGW-1570.

[1] H. K. Moffatt, *Magnetic Field Generation in Electrically Conducting Fluids* (Cambridge Univ. Press, Cambridge, England, 1978).
[2] A. S. Kingsep *et al.*, in *Reviews of Plasma Physics,* edited by B. B. Kadomtsev (Consultants Bureau, New York, 1990), Vol. 16.
[3] S. V. Bulanov *et al.,* Phys. Fluids B **4**, 2871 (1992).
[4] A. Fruchtman, Phys. Fluids B **3**, 1546 (1991).
[5] J. Kalda, Phys. Fluids B **5**, 4327 (1993).
[6] M. A. Berger and G. B. Field, J. Fluid Mech. **147**, 133 (1984).
[7] J. B. Taylor, Phys. Rev. Lett. **33**, 1139 (1974).
[8] J. M. Urrutia and R. L. Stenzel, Phys. Rev. Lett. **62**, 272 (1989).
[9] J. M. Urrutia *et al.,* Phys. Plasmas **1**, 1432 (1994).
[10] T. J. Dolan, *Fusion Research* (Pergamon Press, New York, 1982), Vol. 1, p. 123.
[11] F. F. Chen, Plasma Phys. Controlled Fusion **33**, 339 (1991).
[12] V. A. Osherovich and E. B. Gliner, Solar Phys. **117**, 391 (1988).

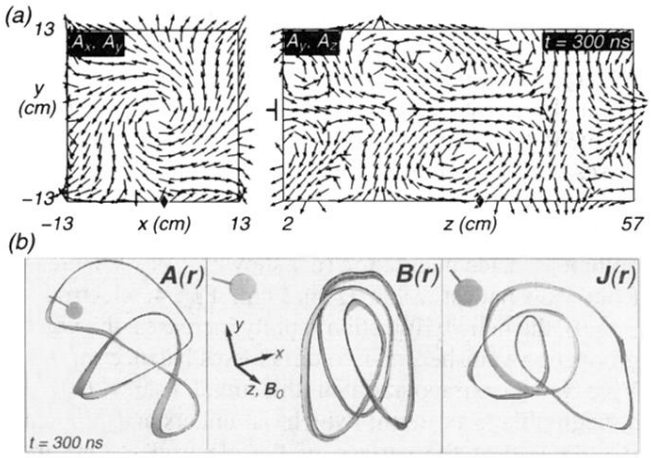

FIG. 2. Field topology of EMHD current pulses. (a) Snapshot of the vector potential field, $\mathbf{A}(\mathbf{r}, t = 0.3\ \mu\text{s})$, displayed as unit vectors in two orthogonal planes (third coordinate indicated by adjacent diamonds). The toroidal field in the transverse x-y plane is due to Hall currents. The solenoidal field in the center of the y-z plane is due to field-aligned currents excited earlier by the electrode. Both fields are linked to form a 3D vortex. A similar topology exists for $\mathbf{B} = \nabla \times \mathbf{A}$ and $\mathbf{J} = \nabla \times \mathbf{B}/\mu_0$. (b) Typical field lines of $\mathbf{A}$, $\mathbf{B}$, and $\mathbf{J}$ in the main vortex ($z \approx 30$ cm) displayed as "sheets" (two adjacent lines connected by a surface) or "tubes" (four lines started on the corners of a square, connected by sheets). The fields are internally twisted, knotted, writhed, and linked with other lines (not shown for clarity), i.e., they exhibit helicity.

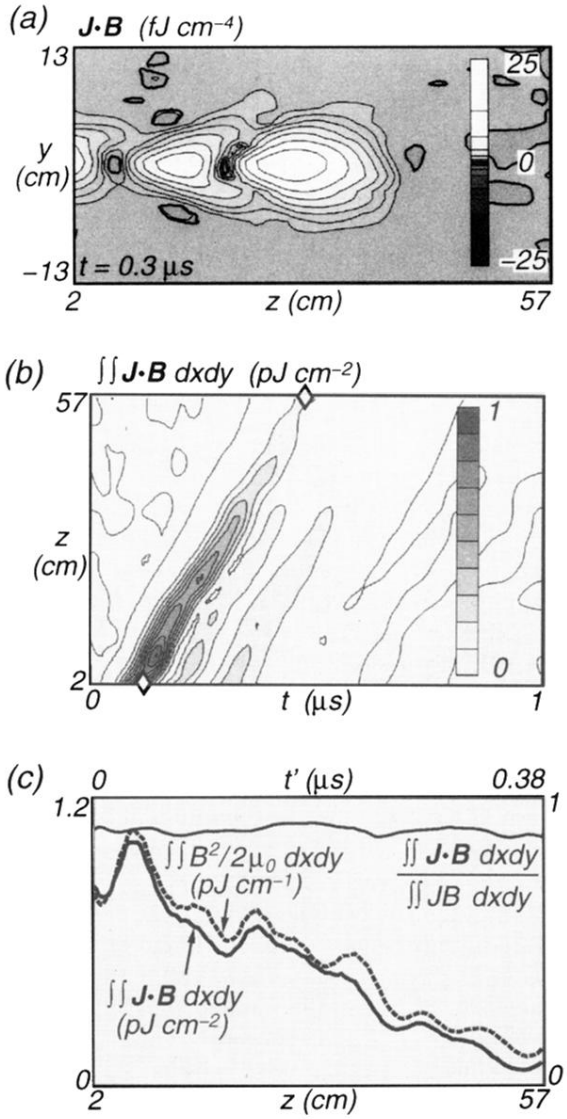

FIG. 3. Helicity density of the vector field $\mathbf{J} = -n_e e \mathbf{v}_e$, showing positive helicity for all current pulses: the primary in the center and induced, secondary ones on the left. The pulses propagate at $v_{\text{whistler}} \approx 1.4 \times 10^8$ cm/s along z ($\| \mathbf{B}_0$) (3 dB = factor of 2 per contour; ± 8 contours; zero contour has double width). (b) Helicity density integrated over transverse cross section showing propagation, damping, and relative helicities of the three pulses. Variation of integration limits (not shown) indicate that damping is *not* due to transverse outflow. (c) Helicity amplitude of the first major pulse along its propagation characteristics, $z = v_{\|} t'$ [straight line between diamonds in (b)]. For comparison, the magnetic energy (dashed line) along the same characteristic is shown and found to exhibit a similar decay. However, the normalized helicity remains constant and close to unity, implying that **J** and **B** are, on the average, well aligned and their topologies do not change due to dissipation.